

Metal-organic frameworks based on pyrazolates for the selective and efficient capture of formaldehyde

Received: 27 October 2023

Accepted: 14 October 2024

Published online: 01 November 2024

Check for updates

Nicolas Sadovnik^{1,2}✉, Pengbo Lyu^{3,4}, Farid Nouar², Mégane Muschi², Menghao Qin⁵, Guillaume Maurin³, Christian Serre²✉ & Marco Daturi¹✉

Indoor air pollution is one of the major threads in developed countries, notably due to high concentrations of formaldehyde, a harmful molecule difficult to eliminate. Addressing this purification challenge while adhering to the principles of sustainable development requires the use of innovative, advanced sustainable materials. Here we show that by combining state-of-the-art spectroscopic techniques with density-functional theory molecular simulations, we have developed an advantageous mild chemisorption synergistic mechanism using porous metal (III or IV) pyrazole- di-carboxylate based metal-organic framework (MOF) to trap formaldehyde in a reversible manner, without incurring significant energy penalties for regeneration. A straightforward, environmentally friendly, and scalable synthesis protocol was established for the porous, water-stable aluminum pyrazole dicarboxylate known as Al-3.5-PDA or MOF-303, capable of functioning as a highly efficient and reusable filter. It demonstrates selectivity and high storage capacity for formaldehyde under conditions typical of severe indoor use, such as in housing or vehicle cockpits, including varying VOC mixtures and concentrations, humidity, and temperature, without any accidental release. Furthermore, we have successfully regenerated this sorbent using a simple domestic protocol, ensuring the material reusability for at least 10 cycles.

Indoor air quality has recently come on the forefront as a major problem for human health. The main indoor pollutant is formaldehyde (FA), widely used but also highly toxic and carcinogenic¹⁻⁴. To date, no efficient remediation techniques exist to eliminate FA with a low energy penalty^{5,6}. Furthermore, the mineralisation of FA at or near room temperature is not viable. Catalysts based on transition metals such as MnO₂, cryptomelane, and mesoporous MnO₂, Co₃O₄, Cr₂O₃ exhibit FA conversion of 50% and 100% at temperatures of around 110 °C and 140 °C, respectively⁷. Improving the catalytic activity at

lower temperatures requires Pt/Pd noble metal catalysts⁷⁻¹¹. However, this approach is hampered by their cost, lack of sustainability and/or thermostability⁷. Room temperature FA removal¹² relies on photocatalysis, which has so far been mainly limited to titania-based substrates, leading to slow and incomplete FA oxidation¹³ in addition to other technical constraints and higher energy consumption. Considering the low FA concentration in indoor air, capture and disposal could be a solution. However, commercial absorbents such as activated carbons and their functionalised versions (*e.g.* amines) are not

¹Université de Caen Normandie, ENSICAEN, CNRS, Laboratoire Catalyse et Spectrochimie, 14000 Caen, France. ²Institut des Matériaux Poreux de Paris, Ecole Normale Supérieure, ESPCI Paris, CNRS, PSL University, 75005 Paris, France. ³ICGM, Univ. Montpellier, CNRS, ENSCM, 34293 Montpellier, France. ⁴Hunan Provincial Key Laboratory of Thin Film Materials and Devices, School of Material Sciences and Engineering, Xiangtan University, Xiangtan 411105, People's Republic of China. ⁵Department of Environmental and Resource Engineering, Technical University of Denmark, 2800 Lyngby, Denmark.

✉ e-mail: nicolas.sadovnik@ensicaen.fr; christian.serre@espci.psl.eu; marco.daturi@ensicaen.fr

efficient enough, particularly in the presence of co-contaminants such as aromatics and humidity^{14,15}. Cationic zeolites possess attractive adsorption properties for a series of volatile organic compounds (VOCs)¹⁶, however, their strong acidic character can induce undesirable modifications of aldehydes e.g. the formation of crotonaldehyde^{17,18}. In addition, while their basic equivalents are more efficient, they are very sensitive to the presence of water and suffer from a high energy penalty to be regenerated¹⁹.

As an emerging class of porous crystalline materials, metal organic frameworks (MOFs) are highly tailorable materials (chemical composition, structure, pore size/shape, nature of active sites), with significant potential for applications in vapour/gas separation processes^{20–24}. Recently, Wang *et al.* reported a mesoporous Cr dicarboxylate MOF, MIL-101(Cr), post-synthetically functionalised with ethylene diamine (ED), demonstrating a FA adsorption capacity up to 5.49 mmol·g⁻¹ in the presence of humidity²⁵. Nevertheless, the practical use of such amine grafted MOFs for FA capture remains doubtful due to their lack of sustainability and high CO₂ affinity. It is expected that under ambient conditions alkyl amines will react with CO₂ to form carbamates^{26,27}, inducing strong competitive co-adsorption amongst other contaminants²⁸. Other research efforts have focused on using amino-based MOFs, such as the work reported by Vikran *et al.*, on the use of the microporous Zr dicarboxylate UiO-66(Zr)-NH₂²⁹. Although good adsorption performances were obtained (despite the consideration of very low humidity condition and with limited adsorption efficiency), the functionalised MOF could not be completely regenerated even with the use of high temperatures (> 130 °C)²⁹. Thus, finding a sustainable and highly selective MOF toward FA adsorption with limited release and easy regeneration still remains a great challenge.

The interactions between pyrazoles and aldehydes have been studied extensively, establishing libraries of chemical intermediates in non-aqueous liquid phase, as part of the Mannich reaction³⁰. Robust metal(II) MOFs are well documented but their constitutive pyrazole groups, once connected to the metal(II) cations, are poorly accessible to guest species. Once pyrazoles are combined with carboxylic groups on the same spacer, one can construct metal(III/IV) water-stable MOFs where the charge-dense cations react with the carboxylic groups, leaving the pyrazole moieties free to interact with guest species^{31–33}. This motivated us to combine experimental and computational approaches to decipher a mild chemisorption mechanism resulting

from the use of ultra-selective FA sustainable metal(III/IV) pyrazole-based MOFs without spontaneous desorption behaviour and energy efficient regeneration (see Fig. 1).

Results and discussion

Formaldehyde capture performance

To address the challenges of selective FA adsorption under ambient conditions, prototypical water-stable and scalable microporous MOFs with commercially available pyrazole dicarboxylate ligands were selected, such as the Zr-MOF denoted Zr-3.5-PDA recently reported as DUT-67(Zr)-PZDC³³ and the Al-MOF denoted Al-3.5-PDA³¹, also recently reported as MOF-303³². CIF files for these materials can be found in the previous references^{31,33}. To facilitate meaningful evaluation of the FA adsorption performance, and to highlight the role of the pyrazole groups, the samples were systematically compared with several microporous materials. This included the amino-functionalised Zr-MOF UiO-66(Zr)-NH₂^{6,34–37}, whose FA sorption ability has been already assessed, the microporous hydrophobic Zr oxide based MOF MIL-140B(Zr)²⁴, that has shown promise for the capture of polar VOCs²⁴. Finally, two different modified activated carbons were used in this study as commercially available sorbent references, specifically used for formaldehyde removal: activated carbon modified with acetacetamide (Modified AC), typically used in domestic applications, and a modified activated carbon used in protection masks of type FA 6075 (6075 AC).

The synthesis protocols and physico-chemical characterizations follow reported procedures for the different MOF materials, with features such as crystallinity and porosity aligning with previously reported data. The pore volume and specific surface area were determined with N₂ adsorption-desorption isotherms data at 77 K, as illustrated in the supporting information (Supplementary Fig. 1). The surface area (obtained using Brunauer-Emmett-Teller (BET) equation) and pore volume for Al-3.5-PDA and Zr-3.5-PDA are 1340 m² g⁻¹ and 0.5 cm³ g⁻¹, and 700 m² g⁻¹ and 0.24 cm³ g⁻¹, respectively. For UiO-66(Zr)-NH₂, the BET surface area was calculated to be 920 m² g⁻¹ with a pore volume of 0.36 cm³ g⁻¹. In the case of MIL-140B(Zr), they accounted for 400 m² g⁻¹ and 0.12 cm³ g⁻¹. For activated carbon (Modified AC), the BET surface area was calculated to be 600 m² g⁻¹ with a pore volume of 0.24 cm³ g⁻¹. Lastly, for the second activated carbon (6075 AC), the surface area was calculated to be 1500 m² g⁻¹ with a pore volume of 0.61 cm³ g⁻¹ (Supplementary Fig. 16). PXRD

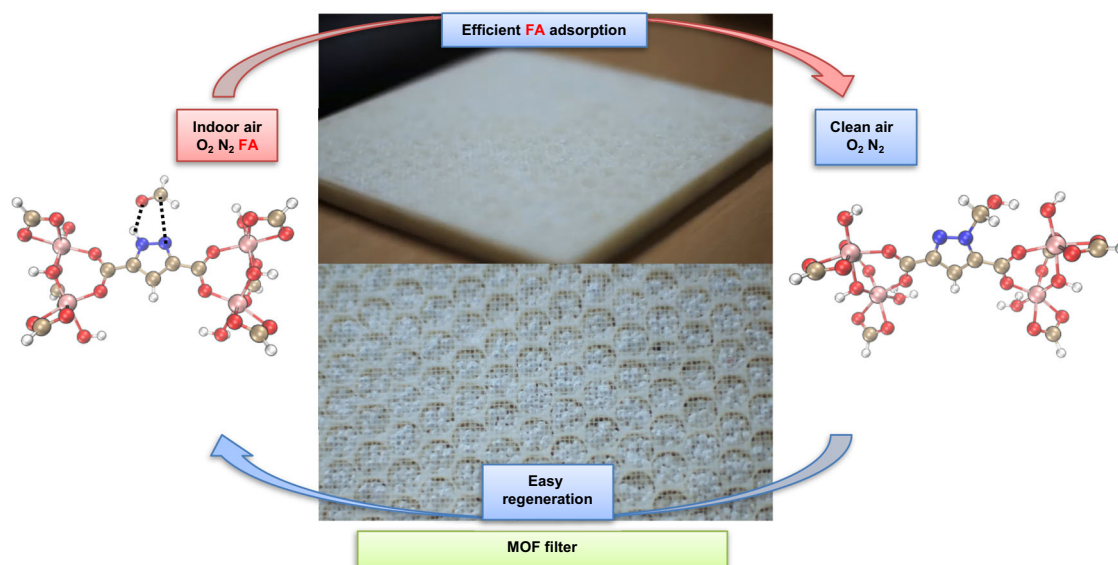


Fig. 1 | Illustration of the selective capture of formaldehyde (FA) using robust pyrazole carboxylate-based MOFs filters. Schematic representation of formaldehyde reversible chemisorption over an Al-3.5-PDA (MOF-303) shaped filter.

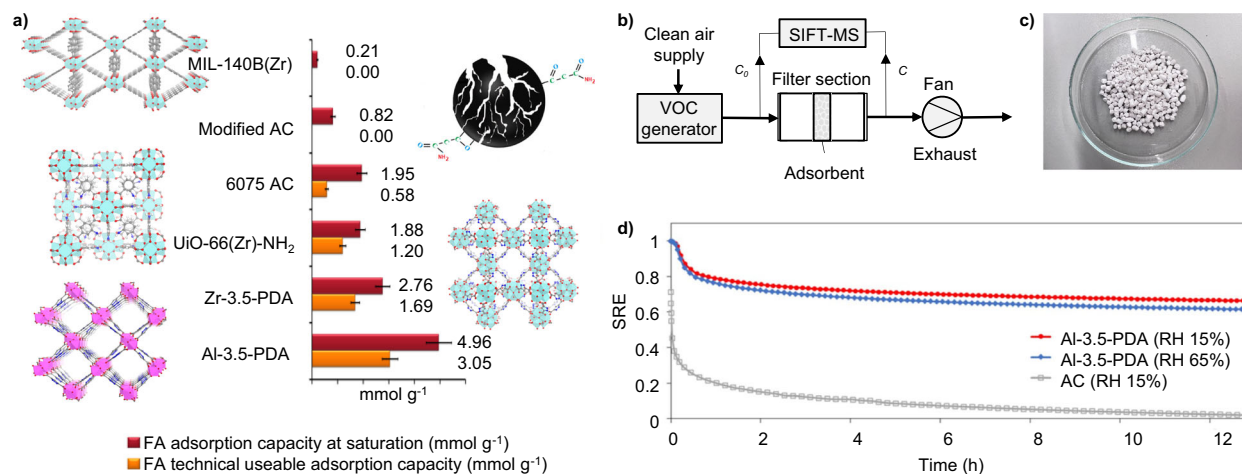


Fig. 2 | Formaldehyde adsorption performances of investigated adsorbents. **a** FA adsorption capacities of the investigated materials at saturation (red bars) and technical useable adsorption capacities (orange bars), measurement error bars \pm 5% in black lines. In the structural schemes, Zr clusters are represented in light blue, whereas Al clusters are in pink; **(b)** Experimental setup for the single-pass

removal test; **(c)** Al-3.5-PDA extrudates; **(d)** FA single-pass removal efficiency (SRE) of shaped Al-3.5-PDA and activated carbon under different relative humidity levels. (test conditions: temperature: 23 °C, flow rate: 74 mL s⁻¹, face velocity: 0.15 m s⁻¹, the mass of adsorbent: 8 g, inlet FA concentration (C_0): 0.2 mg m⁻³ (0.163 ppm)).

experiments and TGA analysis were also performed to confirm the crystallinity and the thermal stability, which were consistent with reported data^{6,34–37}. Details are provided in the supporting information (Supplementary Fig. 1). It is well-known that the adsorption of formaldehyde is enhanced by factors such as a small pore size, a high specific surface area, and a significant microporous volume of the adsorbent. Nonetheless, it is the chemical properties of the adsorbent surface that remain the most pivotal parameter.

To assess the adsorption performances, micro-breakthrough test filtration experiments were initially conducted in a flow of synthetic air, with 90% relative humidity (RH) and 400 ppm of formaldehyde (FA). The concentration of FA was analyzed using mass spectrometry and *operando* infra-red spectroscopy. The FA adsorption saturation capacity for all these MOFs is presented in Fig. 2a, while their breakthrough curves are shown in Supplementary Fig. 2. Where possible, the corresponding technical useable adsorption capacity was also reported, i.e. adsorption capacity when 5% FA is detected in the effluent at the outlet.

The metal pyrazole dicarboxylate MOFs was revealed to exhibit superior properties for FA removal from ambient air. For the Al-3.5-PDA sample, saturation adsorption and technical usable capacities of 5 and 3 mmol g⁻¹ respectively were observed compared to 2.76/1.69 mmol g⁻¹ and 1.88/1.20 mmol g⁻¹ for Zr-3.5-PDA and UiO-66(Zr)-NH₂, respectively. In the case of the hydrophobic MOF MIL-140B(Zr), a negligible amount of adsorbed FA was measured. The modified AC carbon did not exhibit any technically usable capacity when capturing <1 mmol g⁻¹ of FA. However, 6075 AC showed a technically usable capacity of 0.58 mmol g⁻¹ and a saturation adsorption capacity of 1.95 mmol g⁻¹. Both capacities are improved when compared to modified AC, attributed to a better specific surface area. Furthermore, we conducted a comparison of the maximum adsorption concentrations with various materials from the literature, including activated carbons. A detailed summary table can be found in the supplementary information (Supplementary Fig. 11). Our analysis revealed that the pyrazole-carboxylate based MOFs demonstrate remarkable adsorption capacities, reaching levels comparable to some of the most efficient materials known. For instance, it stands in line with polymeric amine-incorporated aminosilicas, which typically exhibit adsorption capacities ranging from 5.2 to 5.7 mmol g⁻¹¹³⁸, as well as post-synthetically functionalised MIL-101(Cr) with ethylene diamine (ED), reaching a capacity of 5.49 mmol g⁻¹¹²⁵. These findings underscore the

promising potential of MOFs for an efficient capture of FA in the presence of humidity, while also revealing the unique ability of the pyrazole-based MOFs to capture and retain exceptional quantities of FA.

In general, modified and non-modified activated carbons exhibit reduced polar VOC adsorption efficiencies and filtering properties with respect to most MOFs, such as recently observed for acetic acid³⁹. In the case of FA removal, our observations highlight that MOFs are excellent candidates for implementing filters with a lower amount of filtering media per gram of adsorbate, as well as increasing the lifetime of filters and protection devices. Specifically, among the different tested MOFs, the lower adsorption affinity of MIL-140B(Zr) is coherent with the lack of functional groups capable of interacting with the hydrophilic FA, which has chemical properties similar to water⁴⁰. In the case of the functionalised activated carbons, they are known to be efficient materials for the adsorption of hydrophobic aromatic compounds⁴¹, similarly as for hydrophobic zeolites⁴⁰. The presence of amino groups allows greater adsorption of FA^{25,29}, however this modification strategy typically fails to prevent the desorption of FA once the temperature rises above 50 °C. This emphasises the need for a material with low or no desorption behaviour near room temperature to ensure safe and efficient performance.

To further assess the FA adsorption performance, FA optical isotherms were performed in a concentration range between 2 and 115 ppm (Supplementary Fig. 3). The calculated Henry's law constant for Al-3.5-PDA was found to be 264 mol kg⁻¹ Pa⁻¹, which is one order of magnitude higher than the value for amino based UiO-66(Zr)-NH₂ of 18.5 mol kg⁻¹ Pa⁻¹²⁹.

However, due to the intrinsic IR characterization limitations, our initial tests were carried out using very high concentrations of FA, significantly exceeding the real conditions of indoor air quality where the FA concentration is usually lower than 1 ppm. Additional tests were further performed to verify the ability of the best performing MOF (Al-3.5-PDA) to efficiently capture FA.

The single-pass removal efficiency (SRE) of a filter packed with Al-3.5-PDA extrudates (Fig. 2b, c) was then measured in a flow of air with 0.2 mg m⁻³ (0.163 ppm) of FA and two levels of relative humidity (15% and 65%). The real-time concentrations of FA at the inlet (C_0) and outlet (C) of the filter were analyzed by selected-ion flow-tube mass spectrometry (SIFT-MS). The single-pass removal efficiency⁴² was calculated as $(C_0 - C)/C_0$. The SRE of a filter packed with the same amount of

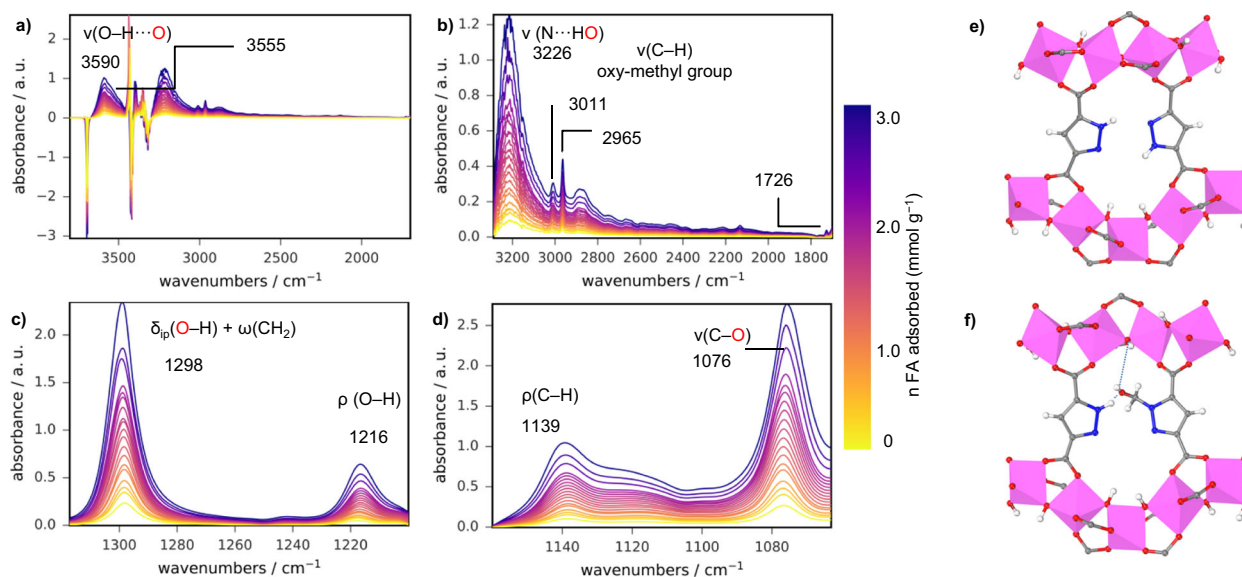


Fig. 3 | FTIR characterisation of the interaction of formaldehyde with Al-3.5-PDA material. **a–c** FTIR spectra recorded after activation of the Al-3.5-PDA sample and the introduction of FA aliquots (from bottom to top, increasing doses of FA aliquots). The spectrum of the activated sample was subtracted. Four main regions were highlighted, from higher (**a**) to lower (**d**) wavenumbers. **e** Al-3.5-PDA MOF

active sites representation. Aluminium, carbon, nitrogen, oxygen and hydrogen atoms are depicted in purple, grey, blue, red and white, respectively. **f** Schematic representation of the interactions between the oxymethyl groups with the neighbouring μ -OH and pyrazole functions via the formation of a double hydrogen bond based on FTIR observations (illustrated by a blue dashed line).

activated carbon was also measured for comparison. The results are presented in Fig. 2d. Shaped Al-3.5-PDA has a higher FA removal capacity than activated carbon in both low and high humidity conditions. The change in relative humidity has little effect on the adsorption performance of Al-3.5-PDA. Remarkably, after 12 h of adsorption, Al-3.5-PDA still exhibits a stable SRE of 66% while the activated carbon was almost saturated. The initial concentration of formaldehyde during these tests corresponds to a high level. In homes with significant formaldehyde emissions from various sources, such as newly constructed or renovated buildings, concentrations varies in Europe from 20–60 $\mu\text{g}/\text{m}^3$ and may exceed 100 $\mu\text{g}/\text{m}^3$ in some specific scenarios⁴³. What is noteworthy is that at the outlet, the concentration falls below the World Health Organization (WHO) threshold of 100 ppb over a 30 min duration. The tests have demonstrated the exceptional ability of this MOF to capture FA in indoor environments, even under high humidity conditions. The SIFT-MS analysis also confirmed that Al-3.5-PDA does not generate byproducts from the FA adsorption process, which is another advantage of this MOF over other solid adsorbents.

These findings clearly demonstrate the superior affinity of pyrazole carboxylate-based MOF materials for the capture of FA, which we attribute, as detailed below, to a unique chemisorption synergistic mechanism.

Chemisorption synergistic FA capture mechanism

Encouraged by the adsorption results, we further investigated Al-3.5-PDA as the most promising metal pyrazole dicarboxylate material for FA capture. In earlier work we developed and patented the Al-3.5-PDA material of formula $\text{Al}(\text{OH})-3,5\text{PDA}$ constructed from Al^{3+} ions and 3,5-PDA = 3,5-pyrazole dicarboxylate ligands³¹. Very recently, Fathieh et al.⁴⁴ reported a structural model for this MOF, denoted MOF-303(Al). Its structure of xhh topology⁴⁴ is built by the assembly of infinite cis/trans chains of corner-sharing $[\text{Al}(\text{OH})]_{\infty}$ octahedra connected by 3,5-pyrazole dicarboxylates through the carboxyl groups, delimiting 1D microporous channels with an average free aperture of 6 Å (Supplementary Fig. 5a) depicting prismatic shaped particle morphologies (Supplementary Fig. 12). Notably, the pyrazole groups are accessible, directed towards the pores and exhibit a distance of

3.86 Å between neighbouring nitrogen atoms. This water stable and scalable MOF, obtained using green ambient pressure conditions, was recently identified as a benchmark material for water harvesting⁴⁵.

The use of in situ FTIR was then considered to gain further insights into the FA adsorption mechanism. The spectrum of the sample presents two bands at 3699 and 3691 cm^{-1} corresponding to the $\nu(\text{O}-\text{H})$ stretches of the μ -OH hydroxyl groups of the infinite chains of the inorganic structure (Supplementary Fig. 5a, c, and d). This suggests the presence of two distinct types of non-equivalent hydroxyls, likely due to the presence of pyrazole ligands. Similar phenomena have already been observed in MOFs presenting both hydroxyl and amino groups, such as MIL-53(Al)- NH_2 , which shows two features at 3700–3693 cm^{-1} and 3660 or 3680 cm^{-1} (the second band being assigned to OH groups interacting with amino groups⁴⁶). Al-3.5-PDA also presents two bands at 3430 and 3416 cm^{-1} associated to the $\nu(\text{N}-\text{H})$ stretches of the pyrazole ligand. The corresponding $\nu(\text{C}-\text{H})$ modes are visible at 3153 cm^{-1} . Those assignments match with density-functional theory (DFT) studies of pyrazole-based compounds⁴⁷. The broad band at 3333 cm^{-1} can be assigned to perturbations of the $\nu(\text{N}-\text{H})$ stretches due to the $\text{N}\cdots\text{HN}$ interactions between the neighbouring pyrazole ligands (hydrogen bonds between the lone pair of the pyridinic nitrogen and the hydrogen of the pyrrolic nitrogen). This assignment is consistent with spectroscopic studies on solid phase pyrazoles reported in the literature⁴⁸. Bands at 1692 and 1337 cm^{-1} are unambiguously assigned to the asymmetric and symmetric stretches of the $(-\text{COO}-)$ carboxylates of the organic ligand chelated to the infinite $[\text{Al}(\text{OH})]_{\infty}$ chains⁴⁶.

To verify the band assignments and the site accessibility deuteration of the sample was performed (see Supplementary Fig. 5 and the related text). Having precise knowledge of the structural properties of the material, the FA/MOF interactions were further examined by in situ IR. FTIR spectra of the sample after introducing CH_2O aliquots are represented in Fig. 3.

Analysis of the IR spectra (Fig. 3c, d) revealed the formation of oxymethyl groups of a primary alcohol by the appearance and build-up of a band at 1076 cm^{-1} , typical of a $\nu(\text{C}-\text{O})$ stretch, as well as a band at 1298 cm^{-1} assigned to the $\delta(\text{OH})$ bending and CH_2 wagging; the in plane bending can be found at 1216 cm^{-1} , while the band at 1139 cm^{-1} is

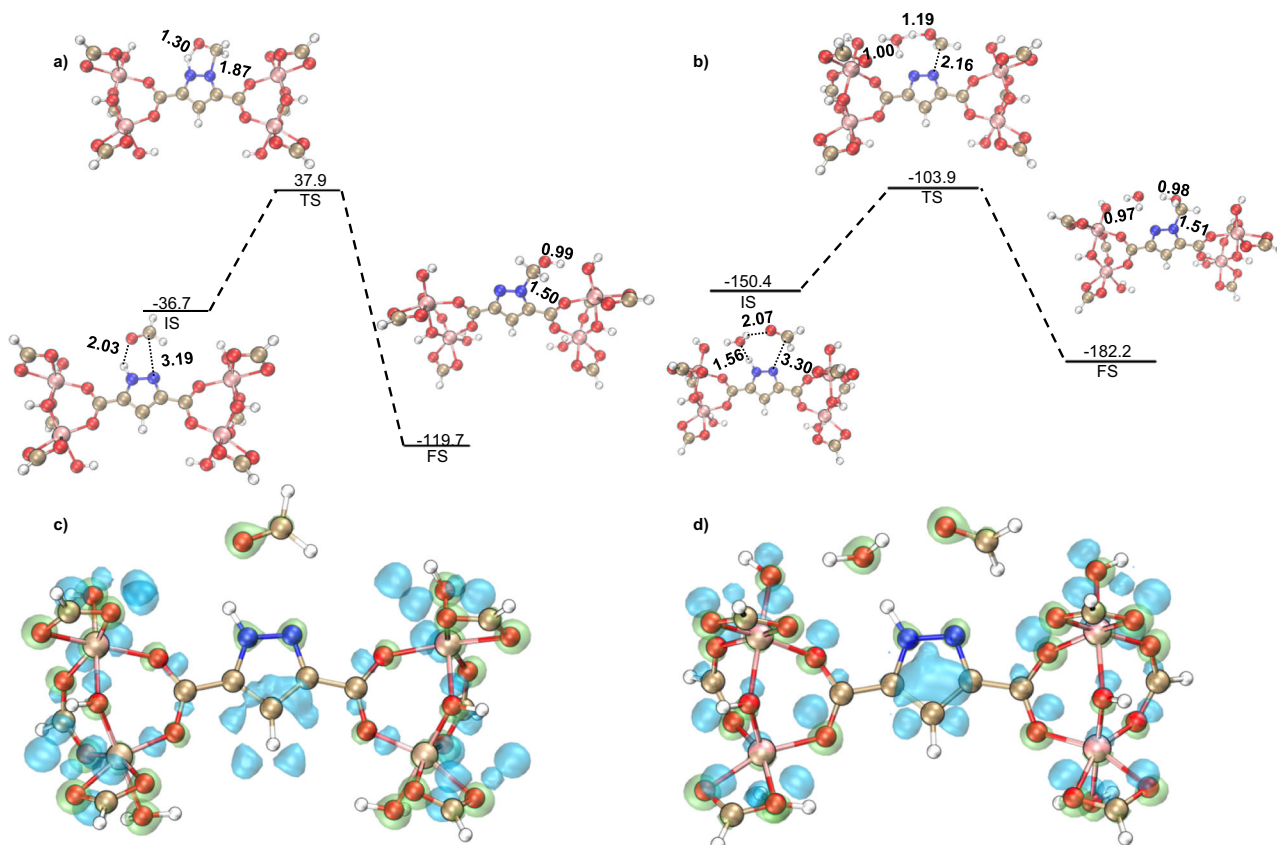


Fig. 4 | DFT-simulated reaction mechanisms for oxymethyl group formation. **a, b** DFT-simulated reaction mechanisms for oxymethyl group formation in absence/presence of H₂O are reported in **(a)** and **(b)**, respectively. The charge difference density plots for their Intermediate states are shown in **(c, d)** with isovalue

of $\pm 0.4 \text{ e} \text{ \AA}^{-3}$, respectively; green and blue colours represent the charge accumulation and depletion regions respectively. Colour code: carbon (tan), oxygen (red), nitrogen (blue), hydrogen (white) and aluminium (pink). All distances indicated are in Å and the energies in kJ mol^{-1} .

characteristic of the rocking mode of $-\text{CH}$ groups⁴⁹. These results strongly support a chemisorption phenomenon of FA upon adsorption on Al-3.5-PDA. This proceeds by the opening of the $\text{C}=\text{O}$ double bond (the associated stretching modes being absent in the spectrum) and an interaction between the carbon of the aldehyde and the pyridinic nitrogen of the pyrazole. Moreover, FA also interacts by hydrogen bonding with the $\mu\text{-OH}$ hydroxyl groups of the inorganic chains, as it can be observed by the progressive decreasing of the $\nu(\text{O-H})$ bands at $3699\text{--}3691 \text{ cm}^{-1}$ (Fig. 3a), the formation of an isosbestic point at 3674 cm^{-1} , and the appearance of the characteristic broad feature at $3650\text{--}3500 \text{ cm}^{-1}$. Concomitantly, a progressive erosion of the $\nu(\text{N-H})$ stretches at $3430\text{--}3416 \text{ cm}^{-1}$ and of the complex envelope at $3338\text{--}3329 \text{ cm}^{-1}$ are observed (Fig. 3b). At the same time, an isosbestic point occurs at 3301 cm^{-1} while a complex band appears at $3289\text{--}3034 \text{ cm}^{-1}$. This is ascribed to the interactions of hydrogen bonding between the formed oxymethyl group and the pyridinic nitrogen. The proximity of the pyrazole groups inside the Al-3.5-PDA framework enables the stabilisation of the oxymethyl by the formation of a double hydrogen bond within the $\mu\text{-OH}$ hydroxyls and the neighbouring pyrazole, as represented in Fig. 3f.

As mentioned above, our findings fit well with analogous phenomena already described at the molecular scale through the formation of stable Mannich reaction intermediates. This occurs via the reaction between FA and pyrazoles in non-aqueous liquid phase³⁰, often used in organic synthesis to protect pyrazoles^{50–52}. However, to the best of our knowledge, this is the first time that such a reaction is reported in gas phase. Therefore, the specific environment of the Al-3.5-PDA pores behave as a nanoreactor to react FA via its pyrazoles groups. Furthermore, this justifies the presupposition of our strategy to coordinate FA

with a carefully chosen coordination site on a customised MOF. Details about the interactions represented in Fig. 3 are provided in Supplementary Fig. 6 and the related text. A summary of the IR bands assigned to the resulting complex is provided in Supplementary Fig. 6e. All the IR assignments and the corresponding species formed are confirmed by the analysis of the reaction on a deuterated Al-3.5-PDA sample (notably the hydrogen bonds, see Supplementary Fig. 7a, b).

To further support our interpretations, DFT calculations were carried out using an extended cluster model containing 4 Al-octahedra (Supplementary Fig. 8a). The adsorption energy corresponding to the most stable configuration of FA interacting over the anhydrous Al-3.5-PDA cluster is $-36.7 \text{ kJ mol}^{-1}$ (Fig. 4a). The distance between the O atom of FA and the H atom of pyrazole is only 2.03 \AA , while the distances of C and H atoms of FA to the N atom of pyrazole are 2.56 and 3.19 \AA respectively, indicating that the $\text{O}\cdots\text{H}$ hydrogen bonding is the main interaction between FA and pyrazole. As shown in Fig. 4c, electrons transfer from the Al-3.5-PDA cluster to the adsorbed FA molecule and they are mainly gained by the O atom of FA ($\Delta q = -0.05 \text{ e}$). On the other hand, upon co-adsorption of FA and H₂O (Fig. 4b and d), the adsorption energy is much higher ($-150.4 \text{ kJ mol}^{-1}$); more electrons are transferred to both O atoms of H₂O ($\Delta q = -0.03 \text{ e}$) and of FA ($\Delta q = -0.08 \text{ e}$), as shown in Fig. 4d. By comparison, alternative MOFs screened by high-throughput computation, showed a moderate heat of adsorption ($40\text{--}50 \text{ kJ mol}^{-1}$) in the best hypotheses⁵³.

We further explored the possible reaction mechanism of FA chemical adsorption in-depth (Fig. 4a). We revealed that the chemical adsorption of FA implies two processes that occur simultaneously at the transition state (TS): (i) the formation of a covalent bond between the carbon of the FA and the pyridinic nitrogen and (ii) transfer of the

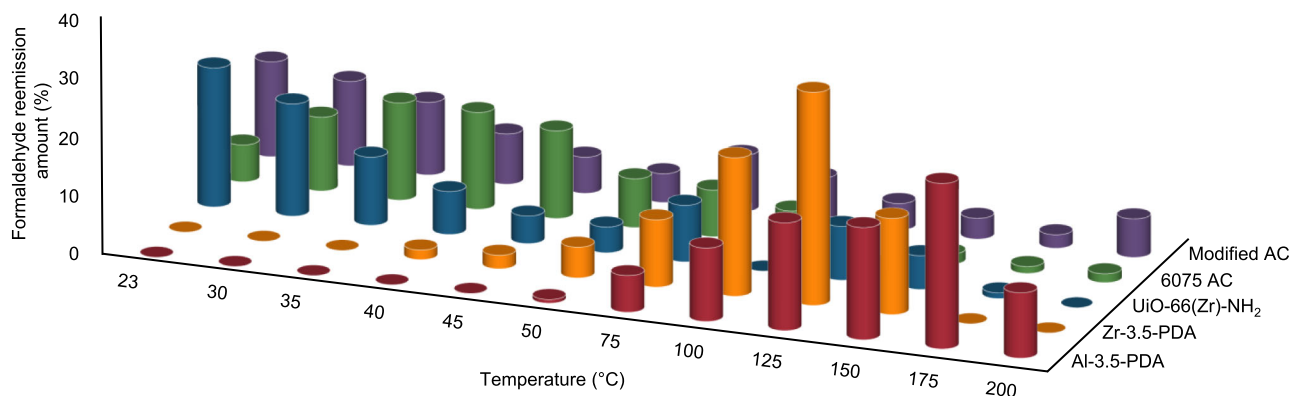


Fig. 5 | Formaldehyde desorption behaviour of investigated samples. Experiments were performed in a flow of clean air, at increasing temperatures.

hydrogen from the pyrrolic nitrogen to the oxygen of FA. A primary alcohol (oxymethyl group) is then formed as the final structure (FS). The theoretical energetic barrier for this reaction is only 74.6 kJ mol^{-1} , rendering it feasible under mild conditions. Additionally, the μ -OH groups show a significant impact on the thermodynamics of this process by stabilising the reaction product via their hydrogen-bonding interactions with the $-\text{CH}_2\text{OH}$ (associated distance of 1.70 \AA). As a consequence, the reaction becomes highly exothermic, releasing 83.0 kJ mol^{-1} . In the presence of water, the mechanism changes significantly (Fig. 4b). In this case, the hydrogen of the pyrrolic nitrogen is transferred to the oxygen of water, while simultaneously another hydrogen is transferred from water to FA, to form a $-\text{CH}_2\text{OH}$ group. The resulting energetic barrier of 46.5 kJ mol^{-1} is significantly lower than in anhydrous conditions. The exothermicity is lowered due to the presence of water but the reaction remains exothermic by 31.8 kJ mol^{-1} . Therefore, the presence of water is expected to facilitate the reaction kinetically while roughly maintaining a similar thermodynamic feasibility. This is in good agreement with our experimental findings showing that the high humidity does not significantly deteriorate the FA removal efficiency of Al-3.5-PDA. This emphasizes that pyrazole-carboxylate based MOFs exhibit site selectivity for formaldehyde over water. It is worth mentioning that the standard enthalpy of the formation of oxymethyl groups calculated by applying IR spectroscopy of adsorbed species at a variable temperature (VTIR) methodology⁵⁴ is found to be -59 kJ mol^{-1} (see Supplementary Fig. 3g), which is in line with DFT calculations qualitatively and temperature programmed desorption (TPD) experiments as shown below (Fig. 5). Also, the atomic distance between the oxygen of the formed oxymethyl group and the oxygen from the μ -OH is experimentally evaluated around 2.7 \AA (see Supplementary Fig. 6f, g and the related text). This is again in good agreement with our DFT cluster-based calculations. However, it is unclear if this mechanism is exclusive of Al-3.5-PDA. To experimentally verify this, we further explored one of its analogues, Zr-3.5-PDA, whose structure is built by $\text{Zr}_6(\mu_3\text{-O})_4(\mu_3\text{-OH})_4$ clusters linked to 8 3,5-pyrazoles dicarboxylic linkers, forming a microporous 3D structure [$\text{Zr}_6(\mu_3\text{-O})_4(\mu_3\text{-OH})_4(\text{PZDC})_6(\text{OH})_4(\text{H}_2\text{O})_4$]. This MOF shows a reo topology with two different types of pores of 16.6 \AA (cuboctahedral) and 8.8 \AA (octahedral)³³. Its structure (Supplementary Fig. 4b) contains accessible pyrazole groups similar to Al-3.5-PDA, therefore a FA chemisorption mechanism is a priori possible. Indeed, similar results are obtained also in this case (Supplementary Fig. 7c–e). However, we noticed that in the Zr-3.5-PDA structure N–N–H and μ -OH groups are geometrically too far from each other³³, making it not as effective as Al-3.5-PDA to capture FA molecules. The reaction mechanism of the FA chemical adsorption process over the representative cluster model of DUT-67-PZDC is illustrated in Supplementary Fig. 13. These DFT calculations shows that the resulting energy barrier is significantly higher for DUT-67-PZDC (67.4 kJ mol^{-1}) compared to MOF-303 (46.5 kJ mol^{-1})

with water. This trend is attributed to the interactions of the FA molecule (adsorbed around N–N–H) with the framework -OH group via the water molecule, which stabilizes the transition state for MOF-303, this specific interaction being absent in DUT-67-PZDC. These computational findings suggest that the adsorption is expected to be more effective for MOF-303 under working conditions with the presence of humidity. This observation explains the slightly lower performance of this Zr MOF in terms of FA adsorption and desorption (Fig. 2). This observation highlights the unique potential of MOFs to immobilise functional groups with a tuneable control of the spatial distribution of the pyrazole functions.

As already mentioned, interactions in the case of amino-based MOF, and more especially in the case of UiO-66-NH₂²⁹, are less effective leading to lower performances in terms of FA affinity. This demonstrates the fundamental importance of structure-properties to achieve ideal capture qualities. Further experimental details on the interaction of UiO-66(Zr)-NH₂ and FA are discussed and provided in SI (see Supplementary Fig. 7f–h and the related text).

Analysis of the reemission and FA capture selectivity

The stability of the different adsorbents was further tested. This is crucial if one wants to regenerate the materials after use to minimise the environmental and economic impact related to replacement of adsorbents in air quality control. A recurrent problem of air filters is the partial release of the adsorbate from the saturated adsorbent once the temperature increases and/or the concentration of the VOC decreases, thus becoming a source of pollution in the environment they are supposed to protect. Therefore, we submitted our materials, which are saturated with FA, to a flow of clean air at increasing temperatures to obtain their thermo-desorption profile. Results are presented in Fig. 5 for the tested materials:

While both tested AC and UiO-66(Zr)-NH₂ materials exhibit significant desorption of FA already at low temperatures ($<50 \text{ }^\circ\text{C}$), the pyrazole-carboxylate based MOFs retain FA up to $50 \text{ }^\circ\text{C}$, before its progressive release close to $200 \text{ }^\circ\text{C}$. This is a ground-breaking result for two reasons: (i) $50 \text{ }^\circ\text{C}$ is the maximum temperature, or even above, what is expected indoor or in a vehicle cockpit exposed to direct sunlight. Therefore, a filter based on these compounds would not spontaneously release the pollutant in the confined environment, maintaining the safety of the users. (ii) In the case of thermally recycling the filter, the required temperature will still be relatively low, so that the energy demand for reusing the filter, e.g. in potential industrial applications, might become competitive compared to the cost of the material itself.

Besides water and FA (the main indoor pollutant), different molecules can be present in the air and might interact with the filter, resulting in changes to the adsorption selectivity. Therefore, we investigated the sorption behaviour of the MOF samples in a mixture of pollutants as well, introducing acetaldehyde and toluene in the flow,

as representatives of the second major aldehyde and aromatic VOCs. In the case of activated carbons (having a major affinity for aromatic compounds), the FA adsorption capacity was reduced almost to zero (Supplementary Fig. 2f–j). Even if FA was pre-adsorbed, toluene was shown to displace it after time under flow conditions. Conversely, MOFs which possess amino or pyrazole groups, showed an excellent selectivity towards FA in the presence of a mixture of water and VOCs (Supplementary Fig. 2f–j). As mentioned earlier, another compound present in high concentrations (400–1000 ppm in the indoor air) and with possible competitive adsorption properties is CO₂. This is especially pertinent in the case of MOFs with amino-compounds, where the amino group is directly bounded to the ligand of the MOF. In such a case the isosteric heat of adsorption of alkyl amines for CO₂ capture is found to be $-(60-90) \text{ kJ mol}^{-1}$ ^{126,27}. It is worth mentioning that the CO₂ isosteric heat of adsorption of Al-3.5-PDA was estimated to be -25 kJ mol^{-1} according to reference⁵⁵, which is considerably lower when compared to that of FA. To further shed light on the possible competition between CO₂ and FA, we also considered the reactivity of pyrazole with CO₂ using the same DFT-cluster model as described above. As shown in Supplementary Fig. 8b, the calculated adsorption energy of CO₂ is only $-24.2 \text{ kJ mol}^{-1}$, indicating its interacting with pyrazole is much weaker. The reaction of CO₂ with pyrazole follows the similar mechanism as FA: the H atom of pyrazole is transferred to an O atom of CO₂ to form a $-\text{COOH}$ group which bonds to the N atom of pyrazole. However, the barrier for this process is as high as $155.7 \text{ kJ mol}^{-1}$ and this reaction is endothermic by 49.9 kJ mol^{-1} . Therefore, CO₂ is not likely to compete with FA. To confirm these assumptions experimentally, we have also investigated by in situ IR spectroscopy the influence of CO₂ on saturated Al-3.5-PDA with FA (See Supplementary Fig. 9 and the related text). The results revealed the absence of any influence of carbon dioxide on the stability of oxymethyl formed compounds.

Thus, Al-3.5-PDA appears to be an excellent candidate for the selective FA capture in real conditions, i.e. in the presence of contaminants such as water, carbon dioxide, and mixtures of other classes of VOCs.

Study of the regeneration and cyclability

Thermal regeneration is commonly used in industry but still incurs a significant energy penalty. Thus, this pushed us to investigate alternative regeneration processes that consume less energy. It is worth noting, while oxymethyl groups are stable in standard relative humidity conditions, the chemisorption in play here is indeed reversible upon washing the sample in water, which leads to an alternative possibility to regenerate MOF-based filters in a sustainable way. To verify this point, we submitted Al-3.5-PDA MOF sample to 10 cycles of saturation and regeneration by soaking in water at room temperature for 3 h (see Supplementary Fig. 10) and room temperature drying (3 h in open air without further temperature increase). As a result, no significant loss of FA capture efficiency was observed: after each water treatment at RT, the sample was shown to completely release the adsorbed FA, as verified by FTIR analysis (Supplementary Fig. 10). The absence of any characteristic bands of chemisorbed FA ($\nu(\text{C}-\text{D})$ at $2300-2050 \text{ cm}^{-1}$) was further identified, as well as a complete regeneration of the bands characteristic of $\mu\text{-OH}$ and $-\text{NH}$ groups. This is consistent with the literature where pyrazole-1-yl-methanol are well known to produce FA in aqueous solution⁵⁶. Therefore, we can infer that liquid water hydrolyses FA chemisorbed on pyrazole groups in the Al-3.5-PDA material. The structural integrity was demonstrated by the preservation of the structural bands in the spectral region between 1700 and 1300 cm^{-1} , with no broadening that would have indicated structural change (Supplementary Fig. 15). Moreover, the X-ray powder diffraction pattern after washing the material for 3 h was comparable to the reference in terms of shape and sharpness (Supplementary Fig. 15), confirming that washing did not significantly impact the

material structure. Additionally, these findings aligned with the material ability to undergo several hundred of water adsorption-desorption cycles, as reported by Hanikel et al.⁵⁷.

Regeneration tests conducted in water at room temperature were performed on self-supported pellets to thoroughly evaluate their recyclability. Moving towards a more stable filter requires the development of a specific shape that can maintain integrity when submerged in water. To tackle this particular challenge, we also evaluated various shaping techniques. The integrity of the shape in liquid water of the Al-3.5-PDA and binder mixture was maintained by using a polymeric binder, polyvinyl butyral (PVB), with a weight percentage ranging from 2 to 10%. Shape integrity was also achieved using poly(vinyl acetate) (PVAc) with a weight percentage $>3\%$. An acceptable specific surface area was achieved using 2% PVB, with only an 8% decrease in the BET surface area (Supplementary Fig. 14). However, the utilization of a high percentage of polymeric binder ($>5\%$) is likely to result in partial blocking or obstruction of porosity, as indicated by the decrease of N₂ adsorption isotherms at 77 K (Supplementary Fig. 14). No structural changes were observed for the shaping (Al-3.5-PDA and 2% PVB) based on FTIR spectra, in particular observing the integrity of the shape of the structural bands in the spectral region between 1700 and 1300 cm^{-1} (Supplementary Fig. 14). In fact, during the collapse of the structure, one would expect to observe a broadening of the structural bands between 1700 and 1300 cm^{-1} , which is not the case here.

Given the high adsorption capacity of this MOF, a filter comprising 200 g of this material is expected to reach saturation after roughly 1 year of continuous usage. Moreover, we should consider the option of regenerating the material in water at room temperature multiple times. As a result, the anticipated lifespan is ~ 10 years, a notably extended duration compared to conventional commercial materials.

This highly selective material for formaldehyde adsorption could offer multifaceted benefits, ranging from improving indoor air quality and protecting human health to facilitating compliance with regulations and enhancing the effectiveness of air purification systems. This material holds promise in addressing formaldehyde-related concerns across various sectors and applications, including air filtration systems (HVAC systems) in offices, schools, hospitals and commercial buildings, as well as sensor applications for formaldehyde detection, where selectivity is essential.

An interesting aspect is the potential combination of activated carbon materials, which are efficient for trapping aromatic compounds, with Al-3.5-PDA material in filtration applications. Such a combination could broaden the spectrum of adsorbed volatile organic compounds (VOCs) while mitigating the re-emission phenomenon associated with traditional activated charcoals. We believe this approach could lead to more effective and versatile air purification solutions.

Finally, through an advanced experimental and computational approach, we report a mechanism for the chemisorption of the noxious formaldehyde relying on metal(III/IV) pyrazole dicarboxylate microporous MOFs). The specific configuration of the pyrazole-based linker near the constitutive OH groups from the inorganic backbone enables synergistic interactions between formaldehyde, free water molecules and the $-\text{NH}$ and $-\text{OH}$ groups from the MOF skeleton leading to exceptional capture efficiency. Consequently, the most efficient material, Al-3.5-PDA, exhibits optimum performance for selective formaldehyde capture and sequestration up to mild temperatures, without sensitivity to humidity (no decrease in adsorption capacity or competitive adsorption) or CO₂ from air, outperforming aromatic amine-based or hydrophobic MOFs and amine-grafted activated carbons. Importantly, if water vapour acts as a reactant for the chemisorption of formaldehyde, liquid water can be used for the reversible release of formaldehyde as an alternative regeneration process at ambient conditions.

Such a selective capture and sequestration efficiency of Al-3.5-PDA towards formaldehyde is inherent to the intrinsic structure and favourable host-guest interactions. This results in an optimum energy

for capture and release at mild temperatures and an easy regeneration by washing with liquid water, paving the way for the development of energy efficient indoor air quality systems. Naturally, there remains work to be done to validate this in real conditions, and ongoing experiments involving adsorption/regeneration cycles on real filters integrated in HVAC systems are in progress. However, at present, this aspect falls outside the purview of this study.

Methods

Synthesis

Al-3.5-PDA (MOF-303). In a typical reaction, 6.00 mmol of 3.5-pyrazoledicarboxylic acid monohydrate and 6.00 mmol of $\text{Al}(\text{OH})_3 \cdot \text{H}_2\text{O}$ are introduced into a 100 mL flask. 60 mL of distilled water is added, and then the mixture is heated to boiling under stirring for 18 h. After filtration, the white solid is washed in 60 mL of distilled water during 5 h at 100 °C, then filtered again and dried in an oven at 100 °C for 2 h.

UiO-66(Zr)-NH₂. The synthesis of UiO-66(Zr)-NH₂ was performed according to reference⁵⁸. Typically, a solution of 15 mL of DMF 1 mmol of 2-aminoterephthalic acid and 1 mmol of ZrCl_4 in 15 mL of DMF was prepared, and heated to 120 °C under stirring for 24 h. The product was then filtered and washed with DMF and ethanol.

Zr-3.5-PDA (DUT-67(Zr)-PZDC). 1.5 mmol of ZrCl_4 and 1 mmol of 3.5-pyrazoledicarboxylic acid monohydrate were mixed together in 8 mL of water and 3 mL of formic acid. The solution was left at room temperature for 72 h under vigorous stirring. The product was then collected by centrifugation, washed with water and ethanol and finally dried under vacuum.

MIL-140B(Zr). MIL-140B(Zr) was prepared following literature procedures²⁴. In a typical reaction, a solution of 2,6 naphthalenedicarboxylic acid (10 mmol), ZrCl_4 (5 mmol), acetic acid (11 mL) and DMF was mixed and kept under reflux for 7 h. After filtration, the white solid was washed with DMF and methanol.

Modified AC. Modified activated charcoal was purchased from Bloow®.

A1 and FA 6075 type AC. The cartridges for protective masks (3 M 6075 A1 and formaldehyde) filter (filter against organic gases and vapors and formaldehyde) were purchased from 3 M Premium Partner Industrie. This protective mask meets the requirements of the following standards: EN 14387:2024 and A1:2008. The activated carbon was removed from the mask and then tested in granular form in micro-breakthrough experiments.

AC. The AC used in the single-pass removal efficiency test was purchased from Xiamen All Carbon Corporation (ACarbon®).

Powder X-ray diffraction. The powder X-ray diffraction analyses were carried out with a Bruker D8 ADVANCE diffractometer in transmission mode; using a $\text{CuK}\alpha$ ray as radiation source ($\lambda = 1.5418 \text{ \AA}$) and a LynxEye detector.

N₂ adsorption/desorption isotherms. The adsorption/desorption isotherms of N₂ were measured at 77 K in an automatic volumetric device (Micromeritics Tristar II). Beforehand, the samples were degassed at 423 K for 8 h under a primary vacuum.

Thermogravimetric analyses

The thermogravimetric analyses on powder, -10 mg, were carried out with a gravimetric analyser (Mettler Toledo TGA 2 STARe System model) in air at a constant speed of 3 °C min⁻¹.

Micro-breakthrough experiments

An *operando* system and an *operando* Sandwich reactor cell were used for these experiments as described in reference⁵⁹. Self-supported pellets of about 20 mg and a surface area of 2 cm² were prepared from the MOFs initially in powder form (pressed at 102 MPa). Materials were activated under argon flow (20 mL min⁻¹) containing 20% O₂ (as in air) at 150 °C during 1 h. Adsorptions experiments were performed at 60 000 h⁻¹ gas hourly space velocity (GHSV), under argon flow (20 mL min⁻¹) containing 20% O₂ and 400 ppm of FA and at 90% RH. FA in the gas phase was generated from a liquid mixture of FA and water (FA 16% by weight), placed in a saturator. The gas flow was analysed by gas phase IR spectroscopy and mass spectrometry (OmniStar GSD 320 mass spectrometer).

Transmission gas-IR spectra were recorded during the adsorption process using a Thermo-Nicolet-6700 Nexus spectrometer equipped with an extended KBr beam splitting device and a mercury cadmium telluride (MCT) cryogenic detector, in the 400–5500 cm⁻¹ range, at 0.25 cm⁻¹ resolution, 64 scans.

The capacity of the adsorbent at saturation and the technical useable capacity were calculated using Eqs. (1) and (2)⁶⁰. The integrals $\int_{t=0}^{t=t_{breakpoint}} \left(1 - \frac{C_{out}}{C^F}\right) dt$ and $\int_{t=0}^{t=t_{sat}} \left(1 - \frac{C_{out}}{C^F}\right) dt$ were calculated by trapeze method⁶⁰.

$$q_{use} = \frac{C^F Q}{10^6 m_s M_{FA}} \int_{t=0}^{t=t_{breakpoint}} \left(1 - \frac{C_{out}}{C^F}\right) dt \quad (1)$$

$$q_{sat} = \frac{C^F Q}{10^6 m_s M_{FA}} \int_{t=0}^{t=t_{sat}} \left(1 - \frac{C_{out}}{C^F}\right) dt \quad (2)$$

Where: q_{use} – Technical useable capacity (mmol g⁻¹); q_{sat} – Capacity of the adsorbent at saturation (mmol g⁻¹); C_{out} – Concentration of FA in the outlet (mg m⁻³); C^F – Feed concentration of FA (mg m⁻³); Q – Volumetric flow rate (mL min⁻¹); m_s – Weight of adsorbent (g); M_{FA} – Molar mass of FA (g mol⁻¹); t – Time (min); $t_{breakpoint}$ – Time when the concentration of FA in the outlet is equal to 5% of the feed concentration; t_{sat} – Time when the concentration of FA in the outlet is equal to the feed concentration.

Formaldehyde reemission

In the case of Al-3.5-PDA; Zr-3.5-PDA and UiO-66(Zr)-NH₂ after reaching the technical useable capacity limit, FA desorption step was performed. In the case of MIL-140B(Zr) and AC desorption step was performed when FA adsorption reached 50% of the capacity at saturation. The sample was then placed under activation flow (total flow: 20 mL min⁻¹, 20% O₂ with argon). Desorption was studied at different temperatures representative of conditions in dwellings or representative of conditions during thermal regeneration: 23 °C, 30 °C, 35 °C, 45 °C, 50 °C, 75 °C, 100 °C, 150 °C, 200 °C. The temperature ramps were 3 °C min⁻¹. The sample was left at different temperatures for 30 min.

The desorbed amount of FA at each temperature (T_i) was calculated using Eq. 3. The integral term was calculated using trapeze method.

$$P_{Ti} = \frac{C^F Q}{10^6 m_s M_{FA} q_{use}} \int_{t=t(T_i)-t_{RMP}}^{t=t(T_i)+30} \left(\frac{C_{out}}{C^F} - 1\right) dt \quad (3)$$

Where: q_{use} – Technical useable capacity (mmol g⁻¹); C_{out} – Concentration of FA in the outlet (mg m⁻³); C^F – Feed concentration of FA (mg m⁻³); Q – Volumetric flow rate (mL min⁻¹); m_s – Weight of adsorbent (g); M_{FA} – Molar mass of FA (g mol⁻¹); t – Time (min); $t(T_i)$ – Starting time at corresponding temperature T_i (min); t_{RMP} – Time for reaching the corresponding temperature T_i (min) (equal to zero for 23 °C);

Optical isotherms

The aforementioned *operando* system was used to produce adsorption isotherms at different temperatures. Self-supported pellets of ~10 mg were prepared from Al-3.5-PDA MOF sample. After thermal activation at 200 °C (1 h), the sample was placed under 20 mL min⁻¹ flow composed of argon, 20% O₂ and a FA concentration between 0.19 and 11.6 Pa, (i.e. between 2 and 115 ppm). The reconstruction of optical isotherms was performed as follows: the sample was left under flow composed of the first minimum concentration of FA for several days (5–6); the equilibrium was considered to have been reached when the species on the surface no longer shows any evolution (the system reached the first equilibrium point). The amount of adsorbed FA was calculated from the surface FTIR spectra and the integration of the area of the characteristic peaks (oxymethyl groups) in the region of ν(CH₂) groups. Following the first point of equilibrium, the concentration of FA in the flow was increased at the following pressure until reaching equilibrium (no evolution of adsorbed species), and so on until completing the isotherm in the considered region. The experiments were performed at 23 °C; 50 °C and 75 °C. The Langmuir⁶¹ (Eq. 4) and Freundlich⁶¹ (Eq. 6) isotherms were fit using gnuplot⁶² fitting algorithm. The Henry's law constant was estimated using Eq. 5 as described in the reference²⁹.

The standard adsorption enthalpy and entropy were estimated using the Variable-Temperature IR (VTIR) plot⁵⁴ (Eq. 7).

$$q_e = \frac{q_{\max} K_L P_i}{1 + K_L P_i} \quad (4)$$

Where: q_e – Sorption capacity (mg g⁻¹); q_{\max} – Sorption capacity at monolayer coverage (mg g⁻¹); K_L – Langmuir constant (Pa⁻¹).

$$K_H = \frac{q_{\max} K_L}{M_{FA}} \quad (5)$$

Where: K_H – Henry's law constant (mol kg⁻¹ Pa⁻¹); q_{\max} – Sorption capacity at monolayer coverage from Langmuir equation (mg g⁻¹); K_L – Langmuir constant (Pa⁻¹); M_{FA} – Molar mass of FA (g/mol).

$$q_e = K_F P_i^n \quad (6)$$

Where: K_F and n – Freundlich constants.

$$\ln\left(\frac{A}{[(A_M - A)p]}\right) = -\frac{\Delta H^\circ}{RT} + \frac{\Delta S^\circ}{R} \quad (7)$$

Where: A – Actual IR absorbance (a.u. cm⁻¹); A_M – Maximum absorbance at full coverage (a.u. cm⁻¹); ΔH° – Standard adsorption enthalpy (kJ mol⁻¹); ΔS° – Standard adsorption entropy (J mol⁻¹ K⁻¹).

Spectroscopic characterisation

Samples were pressed (102 MPa) into self-supported disks (2 cm² area) and placed in a quartz homemade in situ cell equipped with KBr windows for IR measurements during FA adsorption. A movable quartz sample holder allows adjusting the pellet in the infra-red beam for spectra acquisition and displacing it into a heater at the top of the cell for thermal treatments. The cell was connected to a vacuum line for evacuation, calcination steps ($P_{\text{residual}} = 10^{-6}$ – 10^{-9} bar) and for the introduction of FA into the infra-red cell.

Gaseous FA was obtained by thermal depolymerization of paraformaldehyde in a quartz reactor by using a heat-gun at 70 °C. Same method was used to obtain gaseous deuterated FA.

Samples were pre-treated at 250 °C under dynamic vacuum (10⁻⁶ mbar), before adsorption of FA (or deuterated FA) and before deuteration.

FA (then deuterated FA) was adsorbed at room temperature and the pressure of FA (or deuterated FA) inside the IR cell was measured

by a pressure gauge (10⁻⁴–10⁻¹ bar range). Transmission IR spectra were recorded after introduction of FA in the 400–5500 cm⁻¹ range, at 4 cm⁻¹ resolution, 64 scans, on a Nicolet Nexus spectrometer equipped with an extended KBr beam splitting device and a deuterated triglycine sulfate detector (DTGS).

Deuteration of Al-3.5-PDA was achieved by placing the material under gaseous deuterated water with a pressure of 7.0 mbar at room temperature in an in situ cell during 1 h, and then gaseous and adsorbed water were removed by activating the material under dynamic vacuum (10⁻⁶ mbar) at 100 °C during 15 min. Successful water removal as the deuteration was investigated by FTIR. The FTIR spectra were plotted using SpectroChempy⁶³.

Paraformaldehyde (95% purity), deuterated paraformaldehyde (99.8% purity), deuterated water (99.8% purity) were purchased from sigma Aldrich and used without purification.

Regeneration in water at room temperature and cycling

Al-3.5-PDA regeneration was performed on self supported pellet of 20 mg (pressed at 102 MPa) by placing a saturated with deuterated FA pellet of 20 mg in 100 mL of distilled water during a time range between few seconds and 3 h. FA quantities were evaluated using in situ IR methodology. Cycling tests were performed by (i) saturating Al-3.5-PDA pellet with deuterated FA at an equilibrium FA pressure of 0.10 mbar, (ii) placing Al-3.5-PDA pellet in 100 mL of distilled water during 3 h at room temperature and (iii) room temperature drying in the open air without any temperature increase (3 h) and (iv) repeating the procedure 9 times. The amount of adsorbed deuterated FA was calculated from the sample FTIR spectra and the integration of the area of the characteristic peaks (oxymethyl groups) in the region of ν(DH₂) groups. Before each adsorption procedure the complete regeneration was confirmed by the absence of characteristic deuterated FA bands (ν(C–D)) based on the sample FTIR spectra.

Formaldehyde single-pass removal efficiency test

The experiments were conducted in a climate chamber at DTU, where the temperature was maintained at 23 °C ± 0.1 °C, and the relative humidity was accurately controlled at two levels (i.e., dry condition: 15% ± 2%, and humid condition 65% ± 2%). Figure 2b, illustrates the experimental setup, which mainly comprised three components. The VOC generation device will produce a mixed airflow with a set FA concentration of 0.2 mg m⁻³ (0.163 ppm) and flow rate at 74 mL s⁻¹ (face velocity: 0.15 m s⁻¹). The adsorption section comprises a filter containing 8 g of Al-3.5-PDA extrudates, as shown in Fig. 2c. Prior to the tests, the samples were fully activated. Real-time FA concentrations before (C_0) and after (C) the filter were analysed using selected-ion flow-tube mass spectrometry (SIFT-MS). In order to facilitate comparison, the single-pass removal efficiency of an equal amount of activated carbon was also measured.

Shaping

Al-3.5-PDA MOF in a powder form was shaped into extrudates using an extruder (Caleva Multi Lab). Typically, about 18 g of dried and grinded MOF powder as well as 2 g of bentonite binder (10% w/w) were mixed. Water is added to the mixture until a paste is formed. The paste is progressively introduced into the extruder to form extrudates of 2 mm thickness that are manually cut and dried in a vacuum oven at 150 °C for 18 h.

SEM

Scanning Electron Microscopy (SEM) was performed using a FEI Magellan 400 Microscope operating at 20 kV. The MOF powder samples were directly deposited on a carbon-coated aluminium sample holder.

Computational details

All the DFT calculations were based on the use of the B3LYP exchange-correlation functional with TZVP basis set as implemented in the Gaussian 09 program suite⁶⁴. The DFT-D3 method was employed to include the dispersion contribution⁶⁵. The Berny algorithm was used to locate the transition states of the reaction mechanism. Frequency calculations of all optimised structures were performed to ensure no imaginary frequencies were found for minima and only one imaginary frequency found for each transition state. The structure of the extended model was cut from the periodic crystal structure and saturated with terminal water, hydroxyl and formate groups, before being geometry optimised.

Data availability

All data supporting the finding of this study are available from the corresponding authors upon request. Source data are provided with this paper.

References

1. Park, D. W., Kim, S.-H. & Yoon, H. J. The impact of indoor air pollution on asthma. *Allergy Asthma Respir. Dis.* **5**, 312 (2017).
2. Chang, E. T., Ye, W., Zeng, Y. X. & Adami, H. O. The evolving epidemiology of nasopharyngeal carcinoma. *Cancer Epidemiol. Biomark. Prev.* **30**, 1035–1047 (2021).
3. Vardoulakis, S. et al. Indoor exposure to selected air pollutants in the home environment: a systematic review. *Int. J. Environ. Res. Public Health* **17**, 1–24 (2020).
4. Shrubsole, C., Dimitroulopoulou, S., Foxall, K., Gadeberg, B. & Doutsis, A. IAQ guidelines for selected volatile organic compounds (VOCs) in the UK. *Build. Environ.* **165**, 106382 (2019).
5. Luengas, A. et al. A review of indoor air treatment technologies. *Rev. Environ. Sci. Biotechnol.* **14**, 499–522 (2015).
6. Pei, J. & Zhang, J. S. Critical review of catalytic oxidation and chemisorption methods for indoor formaldehyde removal. *HVAC R. Res.* **17**, 476–503 (2011).
7. Bai, B., Qiao, Q., Li, J. & Hao, J. Progress in research on catalysts for catalytic oxidation of formaldehyde. *Cuihua Xuebao/Chin. J. Catal.* **37**, 102–122 (2016).
8. Tan, H. et al. Platinum-supported zirconia nanotube arrays supported on graphene aerogels modified with metal-organic frameworks: adsorption and oxidation of formaldehyde at room temperature. *Chem. A Eur. J.* **25**, 16718–16724 (2019).
9. Guo, J., Lin, C., Jiang, C. & Zhang, P. Review on noble metal-based catalysts for formaldehyde oxidation at room temperature. *Appl. Surf. Sci.* **475**, 237–255 (2019).
10. Guo, Y., Wen, M., Li, G. & An, T. Recent advances in VOC elimination by catalytic oxidation technology onto various nanoparticles catalysts: a critical review. *Appl. Catal. B. Environ.* **281**, 119447 (2021).
11. Mosafa, L., Moghadam, M. & Shahedi, M. Papain enzyme supported on magnetic nanoparticles: preparation, characterization and application in the fruit juice clarification. *Chinese J. Catal.* **34**, 1897–1904 (2013).
12. Tonglu, L. et al. Catalytic oxidation of volatile organic compounds over manganese-based oxide catalysts: Performance, deactivation and future opportunities. *Sep. Purif. Technol.* **296**, 121436 (2022).
13. Chen, R. et al. Photocatalytic reaction mechanisms at a gas-solid interface for typical air pollutant decomposition. *J. Mater. Chem. A* **9**, 20184–20210 (2021).
14. Jo, W. K. & Yang, C. H. Granular-activated carbon adsorption followed by annular-type photocatalytic system for control of indoor aromatic compounds. *Sep. Purif. Technol.* **66**, 438–442 (2009).
15. Zhang, X., Gao, B., Creamer, A. E., Cao, C. & Li, Y. Adsorption of VOCs onto engineered carbon materials: a review. *J. Hazard. Mater.* **338**, 102–123 (2017).
16. Na, C. J., Yoo, M. J., Tsang, D. C. W., Kim, H. W. & Kim, K. H. High-performance materials for effective sorptive removal of formaldehyde in air. *J. Hazard. Mater.* **366**, 452–465 (2019).
17. Diaz, C. D. C., Locatelli, S. & Gonzo, E. E. Acetaldehyde adsorption on HZSM-5 studied by infrared spectroscopy. *Zeolites* **12**, 851–857 (1992).
18. Davydov, A. *Molecular Spectroscopy Of Oxide Catalyst* (John Wiley & Sons, 2003).
19. Qian, H. et al. Adsorption of haloforms onto GACs: effects of adsorbent properties and adsorption mechanisms. *Chem. Eng. J.* **349**, 849–859 (2018).
20. Furukawa, H., Cordova, K. E., O’Keeffe, M. & Yaghi, O. M. The chemistry and applications of metal-organic frameworks. *Science* **341**, 1230444 (2013).
21. Li, J. R., Kuppler, R. J. & Zhou, H. C. Selective gas adsorption and separation in metal-organic frameworks. *Chem. Soc. Rev.* **38**, 1477–1504 (2009).
22. Vellingiri, K. et al. Metal organic frameworks as sorption media for volatile and semi-volatile organic compounds at ambient conditions. *Sci. Rep.* **6**, 1–11 (2016).
23. Maurin, G., Serre, C., Cooper, A. & Férey, G. The new age of MOFs and of their porous-related solids. *Chem. Soc. Rev.* **46**, 3104–3107 (2017).
24. Dedecker, K. et al. Metal-organic frameworks for cultural heritage preservation: the case of acetic acid removal. *ACS Appl. Mater. Interfaces* **10**, 13886–13894 (2018).
25. Wang, Z., Wang, W., Jiang, D., Zhang, L. & Zheng, Y. Diamine-appended metal-organic frameworks: enhanced formaldehyde-vapor adsorption capacity, superior recyclability and water resistibility. *Dalt. Trans.* **45**, 11306–11311 (2016).
26. Darunte, L. A., Walton, K. S., Sholl, D. S. & Jones, C. W. CO₂ capture via adsorption in amine-functionalized sorbents. *Curr. Opin. Chem. Eng.* **12**, 82–90 (2016).
27. Alkhabbaz, M. A., Bollini, P., Foo, G. S., Sievers, C. & Jones, C. W. Important roles of enthalpic and entropic contributions to CO₂ capture from simulated flue gas and ambient air using mesoporous silica grafted amines. *J. Am. Chem. Soc.* **136**, 13170–13173 (2014).
28. Duarte, R., Glória Gomes, M. & Moret Rodrigues, A. Estimating ventilation rates in a window-aided room using Kalman filtering and considering uncertain measurements of occupancy and CO₂ concentration. *Build. Environ.* **143**, 691–700 (2018).
29. Vikrant, K. et al. Adsorption properties of advanced functional materials against gaseous formaldehyde. *Environ. Res.* **178**, 108672 (2019).
30. Hüttel, R. & Jochum, P. Die mannische reaktion der pyrazole. *Chem. Ber.* **85**, 820–826 (1952).
31. Chang, J. S. et al. Adsorbents comprising organic-inorganic hybrid nanoporous materials for sorption of water or alcohol and use thereof. US Patent WO2016186454A1 (2016).
32. Fathieh, F. et al. Practical water production from desert air. *Sci. Adv.* **4**, eaat3198 (2018).
33. Jacobsen, J., Reinsch, H. & Stock, N. Systematic investigations of the transition between framework topologies in Ce/Zr-MOFs. *Inorg. Chem.* **57**, 12820–12826 (2018).
34. Tanada, S., Kawasaki, N., Nakamura, T., Araki, M. & Isomura, M. Removal of formaldehyde by activated carbons containing amino groups. *J. Colloid Interface Sci.* **214**, 106–108 (1999).
35. Wu, L. et al. CNT-enhanced amino-functionalized graphene aerogel adsorbent for highly efficient removal of formaldehyde. *N. J. Chem.* **41**, 2527–2533 (2017).

36. Ma, J. et al. High-performance amino-functional graphene/CNT aerogel adsorbent for formaldehyde removal from indoor air. *Aerosol Air Qual. Res.* **17**, 913–922 (2017).
37. Ewlad-Ahmed, A. M., Morris, M. A., Patwardhan, S. V. & Gibson, L. T. Removal of formaldehyde from air using functionalized silica supports. *Environ. Sci. Technol.* **46**, 13354–13360 (2012).
38. Nomura, A. & Jones, C. W. Enhanced formaldehyde-vapor adsorption capacity of polymeric amine-incorporated aminosilicas. *Chem. A Eur. J.* **20**, 6381–6390 (2014).
39. Severino, M. I. et al. MOFs with open metal(III) sites for the environmental capture of polar volatile organic compounds. *Angew. Chemie. Int. Ed.* **62**, e202211583 (2023).
40. Bellat, J. P., Weber, G., Bezverkhy, I. & Lamonier, J. F. Selective adsorption of formaldehyde and water vapors in NaY and NaX zeolites. *Microporous Mesoporous Mater.* **288**, 109563 (2019).
41. Marsh, H. & Rodríguez-reinoso, F. *Activated Carbon*. <https://www.sciencedirect.com/book/9780080444635/activated-carbon> (2006).
42. Sørensen, S. B., Feilberg, A. & Kasper, K. Removal of volatile organic compounds by mobile air cleaners: dynamics, limitations, and possible side effects. *Build. Environ.* **242**, 110541 (2023).
43. Salthammer, T. Data on formaldehyde sources, formaldehyde concentrations and air exchange rates in European housings. *Data Br.* **22**, 400–435 (2019).
44. Kalmutzki, M. J. et al. Practical water production from desert air. *Sci. Adv.* **4**, eaat3198 (2018).
45. Xu, W. & Yaghi, O. M. Metal-organic frameworks for water harvesting from air, anywhere, anytime. *ACS Cent. Sci.* **6**, 1348–1354 (2020).
46. Hadjiivanov, K. Identification and characterization of surface hydroxyl groups by infrared spectroscopy. *Adv. Catalysis* **57**, 99–318 (2014).
47. Rice, C. A., Borho, N. & Suhm, M. A. Dimerization of pyrazole in slit jet expansions. *Z. fur Phys. Chem.* **219**, 379–388 (2005).
48. Wassermann, T. N., Rice, C. A., Suhm, M. A. & Luckhaus, D. Hydrogen bonding lights up overtones in pyrazoles. *J. Chem. Phys.* **127**, 234309 (2007).
49. Socrates, G. Infrared and Raman characteristic group frequencies. Tables and charts. *J. Raman Spectr.* **35**, 905–905 (2004).
50. Katritzky, A. R., Lue, P. & Akutagawa, K. Formaldehyde: A reagent for simultaneous protection of heterocyclic NH and activation of alternative locations to electrophilic attack. Part II. A new synthetic method for the 5(3)-substitution of N-unsubstituted pyrazoles. *Tetrahedron* **45**, 4253–4262 (1989).
51. Marion, R. et al. Characterization and catecholate oxidase activity of a family of copper complexes coordinated by tripodal pyrazole-based ligands. *J. Inorg. Biochem.* **105**, 1391–1397 (2011).
52. Alkorta, I., Elguero, J., Jagerovic, N., Fruchier, A. & Yap, G. P. A. Study of the structure of 1-hydroxymethylindazole and 1-hydroxymethylbenzotriazole by X-ray crystallography, multi-nuclear NMR in solution and DFT calculations. *J. Heterocycl. Chem.* **41**, 285–289 (2004).
53. Li, W., Liang, T., Lin, Y., Wu, W. & Li, S. In silico screening of metal-organic frameworks for formaldehyde capture with and without humidity by molecular simulation. *Int. J. Mol. Sci.* **23**, 13672 (2022).
54. Garrone, E. & Areán, C. O. Variable temperature infrared spectroscopy: a convenient tool for studying the thermodynamics of weak solid-gas interactions. *Chem. Soc. Rev.* **34**, 846–857 (2005).
55. Li, Z. et al. Constructing multiple sites of metal-organic frameworks for efficient adsorption and selective separation of CO₂. *Sep. Purif. Technol.* **307**, 122725 (2023).
56. Paulus, W. *Microbicides for the Protection of Materials*. 1st edn, Vol. 497 (Springer, 1993).
57. Hanikel, N. et al. Rapid cycling and exceptional yield in a metal-organic framework water harvester. *ACS Cent. Sci.* **5**, 1699–1706 (2019).
58. Banerjee, D. et al. Zirconium-based metal-organic framework for removal of perchlorate from water. *Inorg. Chem.* **55**, 8241–8243 (2016).
59. Thomas, S. et al. Modelling a reactor cell for operando IR studies: from qualitative to fully quantitative kinetic investigations. *Catal. Today* **283**, 176–184 (2017).
60. Leonov, N. et al. *Mass Transfer—Advances in Sustainable Energy and Environment Oriented Numerical Modeling. Mass Transfer*, Vol. 524 (In Tech, 2013).
61. Ayawei, N., Ebelegi, A. N. & Wankasi, D. Modelling and interpretation of adsorption isotherms. *J. Chem.* <https://doi.org/10.1155/2017/3039817> (2017).
62. Williams, T., Kelley, C. & and many others. *GNU PLOT Version 5.2 Patchlevel 8*. http://www.gnuplot.info/ReleaseNotes_5_2_8.html (2020).
63. Traver, A. & Fernandez, C. SpectroChemPy (Version 0.1). *Zenodo* <https://doi.org/10.5281/zenodo.3823841> (2020).
64. Frisch, M. J. et al. Gaussian, Inc., Wallingford, CT. *Gaussian 09 Rev. D.01* <https://www.rsc.org/suppdata/c5/sc/c5sc02423d/c5sc02423d1.pdf> (2016).
65. Grimme, S., Antony, J., Stephan, E. & Helge, K. A consistent and accurate ab initio parametrization of density functional dispersion correction (DFT-D) for the 94 elements H-Pu. *J. Chem. Phys.* **132**, 154104 (2010).

Acknowledgements

Authors acknowledge financial support from the French Agency for the Environment and Energy Management (ADEME) and Teqoya (grant number TEZ17-43). The computational work was performed using HPC resources from GENCI-CINES (Grant A0140907613). We thank S. Dai (IMAP), S. Wang (IMAP) for DUT-67(Zr)-PZDC and UiO-66(Zr)-NH₂ syntheses; P. Bazin (LCS), A. Vimont (LCS) and Y. Levaque (LCS) for technical help with operando and in situ FTIR spectroscopy; E. B. Clatworthy (LCS) for critical discussions and proofreading of the manuscript; P. Guiton (Teqoya) for valuable discussions.

Author contributions

N.S., M.D., and C.S. conceived the research. N.S., F.N., M.M. and M.Q. designed and performed the experiments and analyzed the data. P.L. and G.M. performed and interpreted the computational calculations. N.S. and M.D. wrote the original draft with the help of C.S. All authors contributed in the paper discussion and revision. M.D. and C.S. supervised the project.

Competing interests

The authors declare no competing interests.

Additional information

Supplementary information The online version contains supplementary material available at <https://doi.org/10.1038/s41467-024-53572-z>.

Correspondence and requests for materials should be addressed to Nicolas Sadovnik, Christian Serre or Marco Daturi.

Peer review information *Nature Communications* thanks Hongliang Huang, Fenghai Li and Jianmei Lu for their contribution to the peer review of this work. A peer review file is available.

Reprints and permissions information is available at <http://www.nature.com/reprints>

Publisher's note Springer Nature remains neutral with regard to jurisdictional claims in published maps and institutional affiliations.

Open Access This article is licensed under a Creative Commons Attribution-NonCommercial-NoDerivatives 4.0 International License, which permits any non-commercial use, sharing, distribution and reproduction in any medium or format, as long as you give appropriate credit to the original author(s) and the source, provide a link to the Creative Commons licence, and indicate if you modified the licensed material. You do not have permission under this licence to share adapted material derived from this article or parts of it. The images or other third party material in this article are included in the article's Creative Commons licence, unless indicated otherwise in a credit line to the material. If material is not included in the article's Creative Commons licence and your intended use is not permitted by statutory regulation or exceeds the permitted use, you will need to obtain permission directly from the copyright holder. To view a copy of this licence, visit <http://creativecommons.org/licenses/by-nc-nd/4.0/>.

© The Author(s) 2024